



High temperature spark plasma sintering, a fast and one step route to achieve dense and efficient SrTiO₃-based thermoelectric ceramics

Eliane Bsaibess^{1,2,a} , Florence Moitrier³, Thierry Bourré³, Fabian Delorme^{1,3}, Mustapha Zaghrioui¹, and Fabien Giovannelli¹

¹ Université de Tours, CNRS, INSA CVL, GREMAN UMR 7347, IUT de Blois 15 rue de la chocolaterie, 41029 Blois Cedex, France

² Sciences and Engineering Department, Sorbonne University Abu Dhabi, Al Reem Island, PO Box 38044, Abu Dhabi, United Arab Emirates

³ French-German Research Institute of Saint-Louis, 5 rue du Général Cassagnou, BP 70034, 68301 Saint Louis Cedex, France

Received 22 January 2022 / Accepted 9 April 2022 / Published online 15 April 2022

© The Author(s), under exclusive licence to EDP Sciences, Springer-Verlag GmbH Germany, part of Springer Nature 2022

Abstract (Sr_{0.95}La_{0.05})_{0.95}□_{0.05}TiO₃ ceramics were prepared by solid state reaction and sintered by spark plasma sintering at different temperatures ranging from 1473 to 1873 K for 10 min. The thermoelectric properties show that sintering at temperatures higher than 1773 K allows reaching high thermoelectric properties similar to the ones obtained after annealing at high temperatures in H₂/N₂ for several hours. The high temperature sintered samples exhibit highest power factor near room temperature, resulting in ZT values higher than 0.1. Therefore, the 10 min short SPS process at high temperatures described in this paper is an easy, cheap, fast, and one step route to obtain dense and efficient SrTiO₃-based thermoelectric ceramics. However, SEM observations show that the samples are not pure perovskite phase but contain titanium oxide and lanthanum compound aggregates.

1 Introduction

Since the discovery of the large Seebeck coefficient and electrical conductivity in Na_xCoO₂ by Terasaki et al. [1] in 1997, considerable attention has been given to thermoelectric oxide materials as a promising alternative to current intermetallic compounds, with high potential for future thermoelectric applications due to their abundance, low cost and low toxicity [2, 3]. Such progress in thermoelectric oxides was mainly made for p-type semiconductors, where different cobalt oxides have been discovered and most of them exhibit high figure of merit, i.e., layered cobalt oxides [1, 2, 4–8], perovskite LaCoO₃ [9–12] and rock salt CoO [13]. Considering n-type oxide semiconductors, some promising candidates have been identified such as Al doped ZnO [14], CaMnO₃ [15], substituted SrTiO₃ [16, 17], and such materials remain quite challenging to achieve high thermoelectric performance. Recently, SrTiO₃ compounds have shown great potential as thermoelectric materials [18–20]. SrTiO₃ is a cubic perovskite with ABO₃ structure and traditionally behaves as an insulator. However, through substitutions with a suitable element, it may be converted into a

semiconductor. The efficiency of thermoelectric materials is determined by a dimensionless figure of merit ZT , $ZT = (S^2\sigma/\kappa)T$, where S , σ , κ and T are the Seebeck coefficient, electrical conductivity, thermal conductivity and absolute temperature, respectively. High figure of merit values (≈ 0.3 – 0.4) have been reported in SrTiO₃ sintered in reducing atmosphere (i.e. several hours at high temperatures under flowing Ar/H₂) and substituted on A-site by trivalent elements such as La, Y, Pr, Dy, and Bi [16, 17, 21–25]. Besides, similar ZT values have been recorded when doped with pentavalent elements (Nb and Ta) on B-site [26, 27]. However, owing to its large thermal conductivity, SrTiO₃ is not yet regarded as a practical thermoelectrical material. Therefore, decrease of the thermal conductivity via nanostructuring [28, 29], nano-inclusions [18, 30], as well as through dispersion of nanoparticles [31, 32] have been explored. Unfortunately, despite the decrease of the thermal conductivity, the electrical conductivity also drastically decreases, resulting in a reduced thermoelectric figure of merit. Moreover, the stability of nanostructured materials can also be an issue, especially at high temperatures [33]. Finally, it has been shown that A-site deficiency in SrTiO₃ can simultaneously reduce the thermal conductivity and tune the electrical properties [19, 34–38]. Usually, SrTiO₃-based ther-

^a e-mail: eliane.bsaibess@sorbonne.ae (corresponding author)

moelectric ceramics are first sintered in air and additional high-temperature treatments in reducing atmospheres are required to generate high transport properties [16, 17]. Spark Plasma Sintering (SPS) is a pressure assisted sintering technique [39] allowing fast sintering in reducing conditions due to the atmosphere (vacuum or Ar usually) and the graphite die and punches. SPS has been used to sinter SrTiO₃-based ceramics with high thermoelectric properties [20–24, 40–42]: The highest *ZT* value reported (*ZT*(1073 K) = 1.4) have been measured on ceramics sintered by SPS [43]. Based on the aforementioned considerations, the present study aims to investigate the thermoelectric properties and microstructure evolution of La-doped, A-site-deficient SrTiO₃ ((Sr_{0.95}La_{0.05})_{0.95}□_{0.05}TiO₃) sintered in a short one step process by spark plasma sintering or SPS at different temperatures. Indeed, SPS process proposed in this paper should allow reducing drastically the time spent at high temperatures (from several hours to only several minutes) and avoid the utilization of hazardous gas such as H₂, which could impede mass production of SrTiO₃-based compounds.

2 Experimental section

Dense pellets of (Sr_{0.95}La_{0.05})_{0.95}□_{0.05}TiO₃ were prepared by spark plasma sintering. Commercially available SrCO₃, La₂O₃ and rutile TiO₂ powders with 99.9% purity, purchased from Chempur, were used as raw materials. La₂O₃ was heated at 1273 K for 10 h to remove any trace of La(OH)₃ and La₂(CO₃)₃. For each sample, a stoichiometric amount of precursors was weighted and grounded together for 5 min at 300 rpm in a tungsten carbide planetary ball mill (Retsch PM 100). Following grinding, the resulting mixture was placed in an alumina crucible and calcined at 1473 K for 10 h at a heating rate of 5 K min⁻¹ to ensure the single phase formation. This process was conducted in air in a muffle furnace. After calcination, the obtained powders were white in color.

Sintering was performed using a spark plasma sintering (Syntex 515S- FUJI) apparatus. About 2.2 g of calcined powder were charged into a cylindrical graphite die with a 15 mm diameter. In order to ensure a good electrical contact, a graphite foil was placed between the powder and the graphite die and punches. The A-site deficient La-SrTiO₃ samples were sintered at different temperatures from 1473 to 1873 K at 100 K intervals under the same conditions. According to the corresponding sintering temperature, a constant heating rate of 100 K min⁻¹ was applied and maintained for 10 min under an uniaxial pressure of 80 MPa in argon atmosphere. During the sintering process, the continuous temperature change was recorded by a pyrometer.

The sintered pellets were carefully polished to remove the thin graphite foil and were cut to bar and cuboid shaped samples of dimensions 3 × 3 × 13 mm³ and 6 × 6 × 2 mm³ respectively using a diamond wire saw for measurements of thermoelectric properties.

Other parts were polished for SEM observations. Polishing was performed with a LAM PLAN Masterlam 2.0 polishing machine. Four steps were necessary. Between each step, the sample was rinsed with deionized water and dried with cold air blow. First, the ceramic sample was applied with a load of 27 N on a P400 SiC paper with deionized water for 5 min. The abrasive paper and the sample were rotating synchronically at 300 and 60 rpm, respectively. Second, the ceramic sample was applied with a load of 27 N on an Ultrapad Cloth with MetaDi Supreme 9 μm polycrystalline diamonds suspension (Buehler) for 5 min. The abrasive cloth and the sample were rotating in opposite directions at 150 and 60 rpm, respectively. Third, the ceramic sample was applied with a load of 27 N on a Verdutex Cloth with MetaDi Supreme 3 μm polycrystalline diamonds suspension (Buehler) for 5 min. The abrasive cloth and the sample were rotating synchronically at 150 and 150 rpm, respectively. And fourth, the ceramic sample was applied with a load of 25 N on a ChemoMet Cloth with MasterMet 0.06 μm amorphous colloidal silica suspension (Buehler) for 10 min. The abrasive cloth and the sample were rotating in opposite directions at 150 and 150 rpm, respectively. Finally, the sample was rinsed with deionized water and then soaked in a deionized water and citric acid solution in an ultrasonic bath for 15 min and dried with cold air blow.

The apparent densities and porosities of sintered ceramics were calculated from the pellets weight and dimensions. Phase purity was analysed by powder X-ray diffraction (XRD) with Cu Kα radiation (λ = 1.5418 Å) using a Bruker D8 advance diffractometer, in the range of 20° to 80° (2θ) with a step of 0.02° and a counting time of 0.5 s per step at room temperature.

The scanning electron microscopy (SEM) observations have been performed using FEI Nova NanoSEM 450 field emission SEM coupled with an Energy Dispersive Spectrometer (EDS Bruker Quantax). As the samples are supposed to be conductive, no coating has been deposited on the sample surfaces prior observation.

The thermoelectric measurements on bar-shaped samples, including the electrical conductivity and the Seebeck coefficient were simultaneously performed in the temperature range of 400–1000 K using a ULVAC ZEM-3 equipment. Thermal diffusivity measurements of cuboid shape specimens were carried out using a laser flash system (Netzsch LFA 457) in vacuum. Three measurements were conducted at each temperature, in between 400–1000 K, in order to assess the reproducibility. Both surfaces were coated with a thin layer of graphite to increase the absorption of infrared radiation energy. Specific heat capacity measurements were carried out by Differential Scanning Calorimeter (DSC, Netzsch STA 449 F3 Jupiter) in a continuous-heating mode of 20 K min⁻¹ up to 1000 K using 50 mg of powdered sample introduced into platinum crucibles. Based on the above measured parameters, the thermal conductivity (κ) was calculated from the product of the thermal diffusivity (D), the specific heat capacity (c_p)

and the bulk density ρ . In this study, the estimated measurements uncertainties are evaluated according to Alleno et al. [44].

3 Results and discussions

After sintering, ceramics were highly dense with relative densities about 99.9% of the theoretical value for $\text{Sr}_{0.95}\text{La}_{0.05}\text{TiO}_3$ compound (the theoretical value is 4.863 g cm^{-3}) [45]. This is consistent with previous works that achieve dense ceramics by SPS at 1473 K [20, 46]. In this work, the chosen maximal temperature is between 1473 and 1873 K, i.e. higher than the temperature requested for densification. Besides density, the color of the final ceramics drifts from mid-grey to dark grey with increasing sintering temperature. The XRD analyses of the samples at different sintering temperatures are illustrated in Fig. 1. According to the XRD patterns of the sintered pellets, it is found that there is no change of the main phase, cubic SrTiO_3 with Pm3m space group, during the sintering process [PDF: 00-035-0734]. Besides, some additional small diffraction peaks are detected as shown in the insert of Fig. 1. When the material is sintered at 1473 K, a weak diffraction peak marked by (o) symbol appears at $2\theta \approx 27.2^\circ$. Loland et al. [46] and Singh et al. [20] have attributed this peak to TiO_2 rutile structure [PDF:04-003-0648]. However, with increasing sintering temperature, this peak disappears markedly. Moreover, a second weak diffraction peak is detected at $2\theta \approx 29.3^\circ$. Singh et al. [20] have attributed this peak to $\text{La}_2\text{Ti}_3\text{O}_9$ [PDF:01-075-4857]. However, it may also corresponds to lanthanum-containing compounds such as $\text{La}_2(\text{CO}_3)_3 \cdot 8\text{H}_2\text{O}$ [PDF:00-025-1400] or La_2O_3 [PDF:01-071-5408], as well as a structure of reduced titanium dioxide such as Ti_9O_{17} [PDF:00-050-0791]. However, these peaks remain close to the detection limit and further investigations by scanning electron microscopy have been performed.

Whereas the density of all the ceramics is high (> 99.9 % RD), backscattered-electron (BSE) images (Fig. 2a) exhibit a large number of black spots that could be pores. However, secondary electron images (Fig. 2b) show that most of these features are not pores but grains.

EDS analyses show that these grains are titanium and oxygen rich (data not shown). This is consistent with the presence of titanium oxides as observed in XRD patterns. These grains are present in all the samples. As the XRD peaks for rutile are only present in the sample sintered at 1473 K, it probably means that the peak at 29.3° is at least related to some titanium suboxides.

Another interesting feature is the presence of randomly distributed white areas (Fig. 3a) in samples sintered at 1473 K. EDS analyses show that these white areas are composed by aggregates containing at least lanthanum and oxygen (Fig. 3b–d). Therefore, there is probably a contribution of lanthanum containing com-

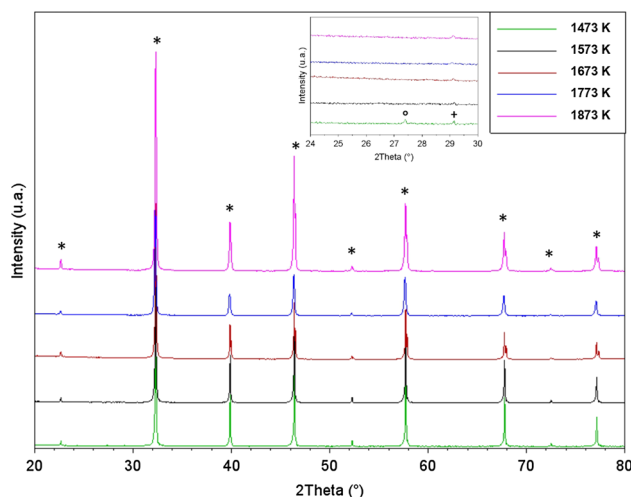


Fig. 1 XRD patterns of 5% deficiency pellets sintered at different temperatures. The marks in the insert point to a secondary phase of: TiO_2 (o) and Ti_9O_{17} and/or $\text{La}_2(\text{CO}_3)_3 \cdot 8\text{H}_2\text{O}$ (+)

pounds to the small 29.3° XRD peak. However, as these areas don't exhibit significant amount of titanium, the presence of $\text{La}_2\text{Ti}_3\text{O}_9$ compound as reported by Singh et al. [20] can be ruled out. Figure 3b demonstrates that perovskite grains around these aggregates are smaller (200–300 nm) than grains not in their vicinity (700 nm–1.5 μm).

The sample sintered at 1573 K exhibits a similar kind of microstructure. However, lanthanum compound aggregates show clear reaction aureole (Fig. 4a). The perovskite grains around the lanthanum compound aggregates exhibit a “core-shell like” microstructure (Fig. 4b) similar to the one described by Dehkordi et al. [47] for Pr substituted SrTiO_3 samples sintered by SPS at 1673–1773 K for 5 min with a heating rate of 300 K min^{-1} . It is interesting to note that in $\text{Sr}_{0.95}\text{La}_{0.05}\text{TiO}_3$ samples prepared by the same methods, these authors didn't observe such features. EDS analyzes clearly show that the rim contains lanthanum whereas it is not clear for the core. According to Dehkordi et al. [47], Pr was found in both core and rim but in higher concentration in the rim. However, in their study, the Pr concentration was usually higher than the La concentration used in the present study. Finally, Dehkordi et al. [47] didn't mention the presence of titanium oxides but some dark spots on their SEM images could be attributed to their presence. Moreover, the perovskite grains around the lanthanum compound aggregates seem to be slightly larger (300–800 nm) whereas the size of other perovskite grains doesn't significantly change compared to the sample sintered at 1473 K.

The sample sintered at 1673 K exhibits a different kind of microstructure as grain growth starts to occur. The perovskite grain size is in the range 1–5 μm (Fig. 5a). Therefore, most of the lanthanum compound aggregates are located inside perovskite grains. More-

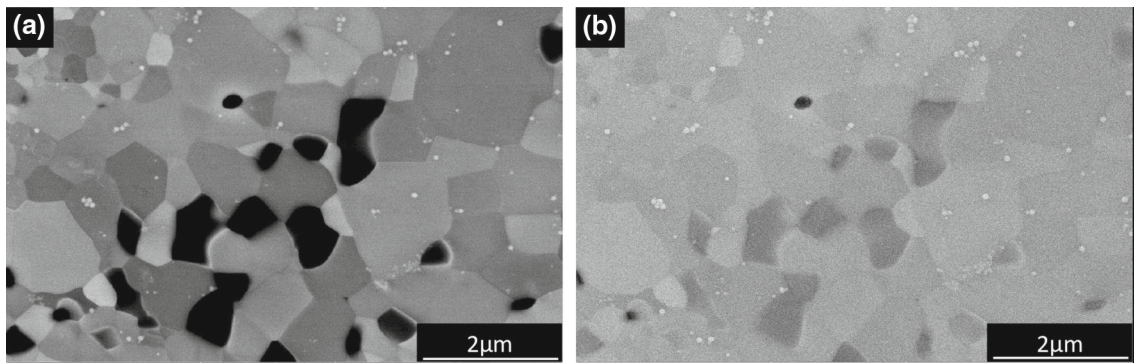


Fig. 2 SEM images of the polished ceramic sintered at 1573 K, **a** backscattered-electrons (BSE) and **b** secondary electrons (SE)

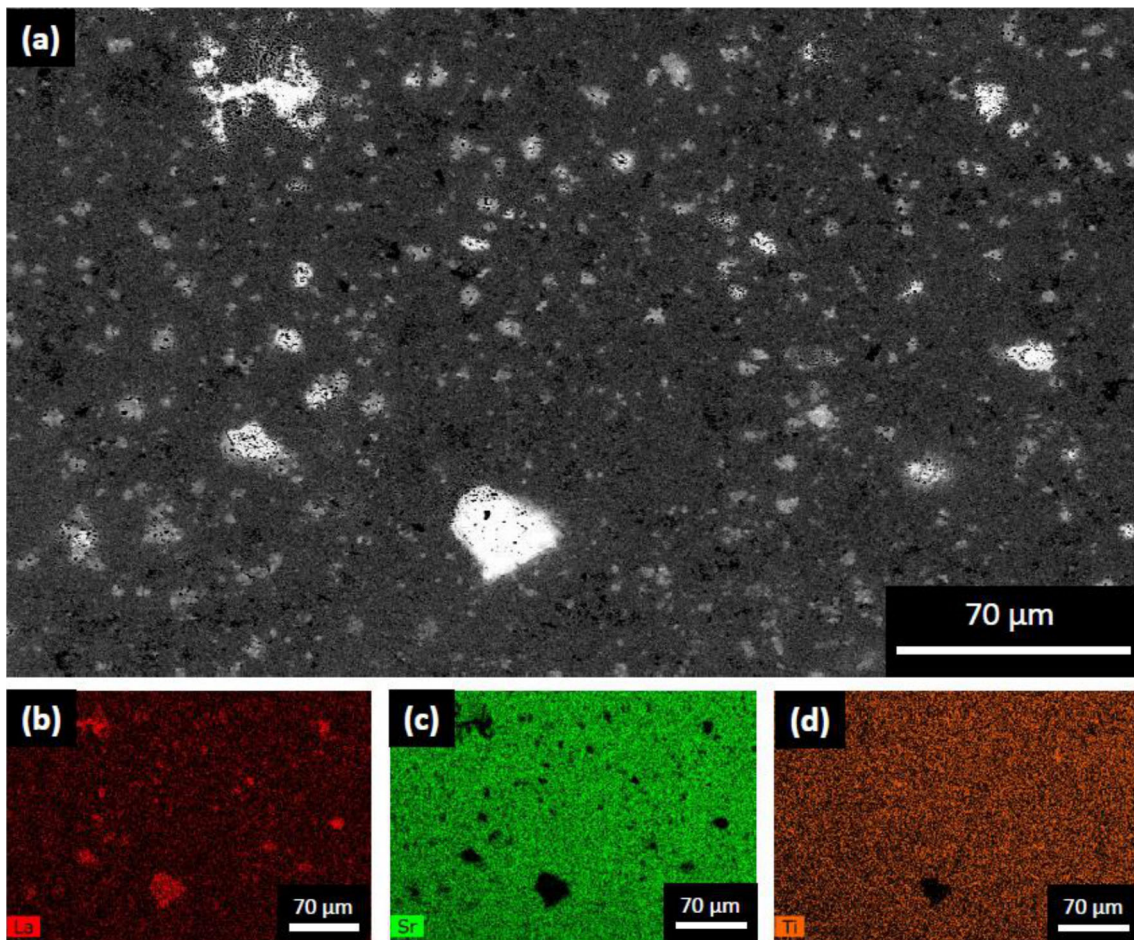


Fig. 3 SEM images of the polished ceramic sintered at 1473 K showing, **a** the distribution of white areas (BSE image), **b** the EDS lanthanum mapping of the same area, **c** the EDS strontium mapping of the same area, **d** the EDS titanium mapping of the same area

over, some grains with “core-shell-like” microstructure can still be observed. In the sample sintered at 1773 K, perovskite grains exhibit a size between 2 and 20 μm (Fig. 5b). Grains with “core-shell-like” microstructure have disappeared and lanthanum compound aggregates are located inside perovskite grains. Small titanium oxide grains are always associated with lanthanum compound aggregates, whereas larger ones lie at the boundaries of the perovskite grains.

The microstructure of the sample sintered at 1873 K is similar (Fig. 6a) but with even larger perovskite grains (6–40 μm). Figure 6b shows that the lanthanum compound aggregates are still well dispersed within the sample.

Vickers microhardness (Buehler Wilson VH1202) was measured at room temperature on the polished ceramics. Microindentation measurements with several loads were performed to determine the constant plateau hard-

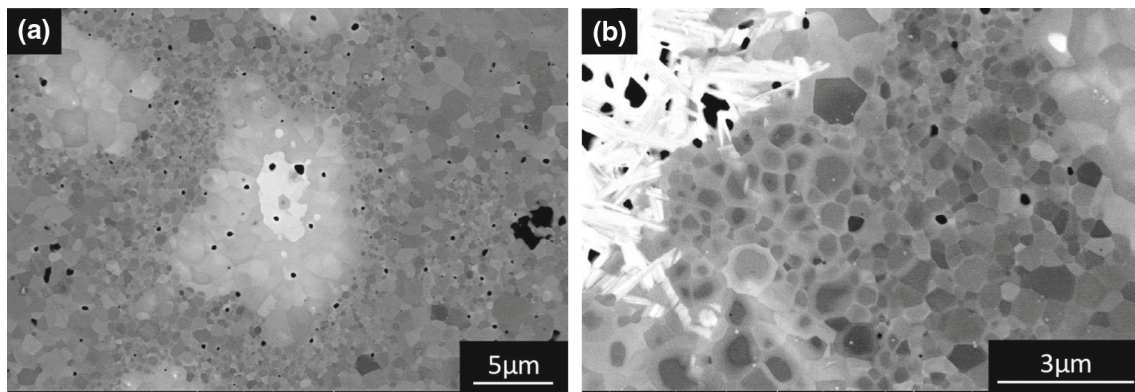


Fig. 4 BSE images of the polished ceramic sintered at 1573 K showing, **a** the reaction aureole around lanthanum compound aggregates and **b** the “core-shell-like” microstructure of the small grains in the vicinity of lanthanum compounds

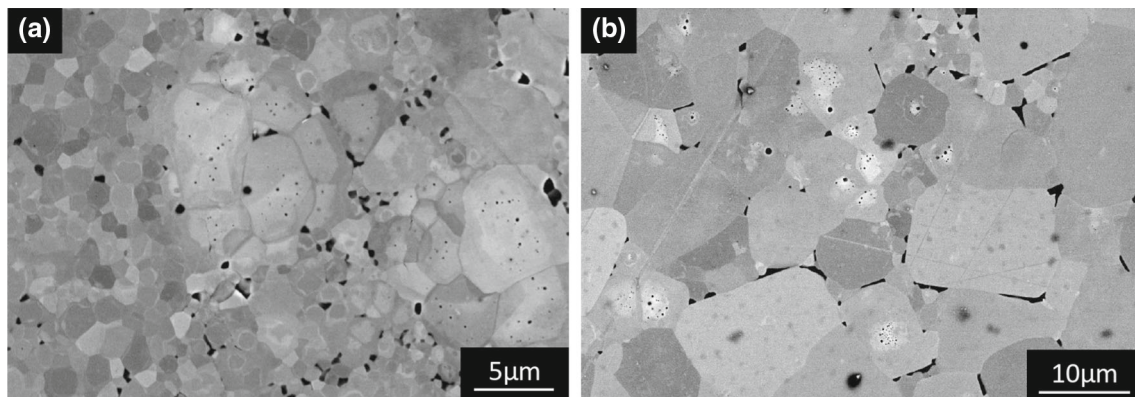


Fig. 5 BSE image of the polished ceramic sintered, **a** at 1673 K showing grain growth, lanthanum compound aggregates inside large perovskite grains, grains with “core-shell-like” microstructure and titanium oxides and **b** at 1773 K showing large perovskite grains

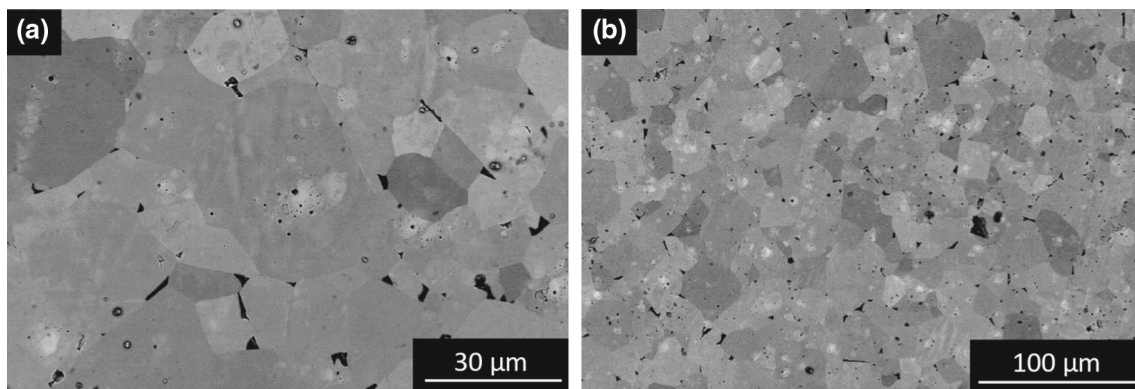


Fig. 6 BSE images of the microstructure of the polished ceramic sintered at 1873 K showing, **a** large perovskite grains and **b** the distribution of the lanthanum compound aggregates

ness. The given microhardness value is the average of six measurements with a load of 0.1 kgf, corresponding to the constant plateau hardness for the samples for 10 s.

Loland et al. [46] reported that some of their samples sintered by SPS were brittle and broke into several pieces when machined. No similar behavior was observed in this study, but the hardness of the samples sintered at 1473 and 1773 K was measured. The later exhibits a lower hardness compared to the one sintered

at 1473 K, 8.9 and 6.0 GPa, respectively. This could be related to the lower oxygen content in the sample sintered at 1773 K. However, these values are consistent with the 7.7 GPa Vickers Hardness reported for pure SrTiO_3 ceramics [48] or the 9.8 to 9.2 values reported for Tm-substituted SrTiO_3 ceramics [49].

In order to evaluate the potential for thermoelectric applications, a systematic study of the compounds prepared has been undertaken to assess simultaneously the electrical conductivity and Seebeck coefficient.

Figure 7a shows the temperature dependence of electrical conductivity (σ) of ceramics sintered at different temperatures.

For all sintered ceramics, in the whole measuring temperature range (from 400 to 1000 K), the electrical conductivity σ decreases with increasing temperature indicating a metal behavior. Moreover, increasing sintering temperature significantly raises the electrical conductivity σ of the samples sintered at 1673 K and above over the whole measuring temperature range (at 400 K, 2×10^3 , 2.5×10^4 and 8×10^4 S m⁻¹ for the samples sintered at 1473, 1673 and 1873 K respectively). The highest value measured in this study is still lower than the one reported by Acharya et al. for Nb-doped SrTiO₃ + 1% graphite (3.2×10^5 S m⁻¹ at 500 K) [43].

Figure 7b illustrates the temperature dependence of the Seebeck coefficient for all sintered ceramics. All samples exhibit a negative value of the Seebeck coefficient over the whole examined temperature range, indicating *n*-type conduction. As can be seen from Fig. 7b, the Seebeck coefficient of the pellets sintered at 1473 K remains nearly constant (≈ -350 μ V K⁻¹) over the whole temperature range, whereas sintering above 1473 K dramatically decreases the Seebeck coefficient down to -150 μ V K⁻¹ for the samples sintered at 1673 K and above. Moreover, increasing the sintering temperature above 1673 K does not seem to significantly affect the Seebeck coefficient value. For metal or degenerated semiconductors, the Seebeck coefficient is defined according to the following equation [50]:

$$S = \frac{8 \pi^2 k_b^2}{3 e h^2} m^* T \left(\frac{\pi}{3 n} \right)^{2/3} \quad (1)$$

where n , k_b , m^* and h are the carrier concentration, Boltzmann constant, effective mass and Planck constant respectively. Hence, Seebeck coefficient is inversely proportional to the carrier concentration. It is difficult to understand clearly the behavior of these samples properties. Indeed, they are probably related to the oxygen vacancies created due to high temperature sintering, but some contribution of the lanthanum concentration within the perovskite phase or its amount, size, nature and/or distribution as well as those of titanium oxide phases could be significant. However, an interesting feature can be observed for samples sintered at 1673, 1773 K and 1873 K. Indeed, these three samples exhibit similar Seebeck coefficient values but increasing electrical conductivities with sintering temperature. Moreover, since the Seebeck coefficient is inversely proportional to the carrier concentration, this means that once the temperature exceeds 1673 K, the charge carrier concentration is constant. In the same time, as the electrical conductivity increases, the temperature of sintering probably leads to an increase of charge carriers mobility. A similar behavior has been recently reported by Cao et al. [51] for samples sintered with green body embedded in sacrificial carbon powder bed. These authors have attributed such behavior to changes in the grain boundary properties. It is possible that the

graphite dies and punches used for spark plasma sintering play a similar role as their sacrificial carbon powder bed. Srivastava et al. [19] in samples reduced in Ar/H₂ for 24 and 48 h and Kovalevsky et al. [38] in conventionally sintered Nb-doped A-deficient SrTiO₃ also noticed an increase of charge carriers mobility.

The calculated power factor of the as-sintered ceramics is presented in Fig. 7c, showing a temperature dependent thermoelectric performance. As reflected by the electrical conductivity and Seebeck coefficient, the power factor of studied compounds increases with rising sintering temperature and the highest recorded value is 2×10^{-3} W m⁻¹ K⁻² at 400 K for the compound sintered at 1873 K. According to the previous studies [23], owing to their high density, the obtained ceramics have extremely large electric conductivity which resulted in high power factors. The experimental results of this study compared to previous studies, also using SPS, show a similar behavior of the power factor as function of the sintering temperature. In this regard, recent studies have reported, on the same class of materials, a value close to 1 mW m⁻¹ K⁻² on (La_{0.12}Sr_{0.88})_{0.95}TiO_{3- δ} [20], 0.6 mW m⁻¹ K⁻² on Nb doped SrTiO₃ [52], 1.2 mW m⁻¹ K⁻² on Sr_{0.8}La_{0.13}Ti_{0.95}Nb_{0.05}O₃ [53] and 1.6 mW m⁻¹ K⁻² on Sr_{0.94}Ti_{0.8}Nb_{0.2}O_{3 \pm δ} [34] at 400 K. Consequently, the optimum sintering temperature for A-site deficient La-SrTiO₃ ceramics sintered by spark plasma route is considered as 1873 K to achieve maximum power factor value. The power factor observed in this work is among the highest recorded values to date for oxides near room temperature [43]. Hence, a short high temperature SPS treatment appears as a good strategy to achieve high thermoelectric performance.

The thermal conductivity of the as-sintered ceramics was evaluated and showed in Fig. 8a. Obviously, it was found that the thermal conductivity decreases with increasing temperature due to the enhancement of the phonon–phonon interactions (Umklapp process [54]). Thermal conductivity does not exhibit a clear trend versus the sintering temperature: indeed, the lowest thermal conductivity is measured for the sample sintered at 1573 K whereas the highest is for the sample sintered at 1873 K; It is probably due to the fact that the samples are not pure phase but composites with varying phases nature, amounts and grain size. Therefore, many parameters can contribute positively or negatively to the total thermal conductivity. However, it seems that the samples sintered at 1673 K and above exhibit slightly higher thermal conductivity. This could be due to their higher electrical conductivity and the larger grains. κ_L , the lattice part of thermal conductivity (Fig. 8b) calculated using the Wiedemann–Franz law ($\kappa_e = \sigma L T$ with T the temperature, $L = 2.45 \times 10^{-8}$ Ω K⁻² and $\kappa = \kappa_L + \kappa_e$), clearly demonstrates that samples sintered at 1573 and 1873 K exhibit similar values and that the values for other samples are not significantly different. The thermal conductivities of the samples sintered at high temperature are higher than those reported for A-deficient conven-

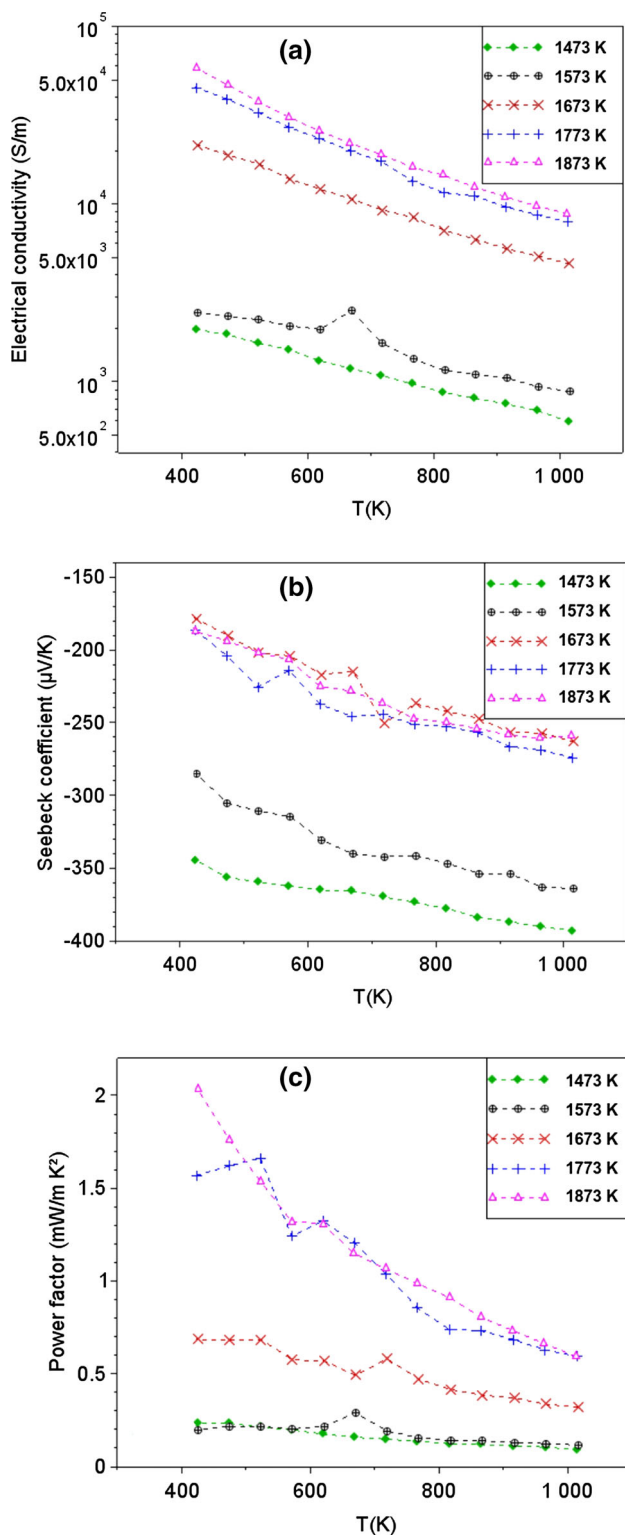


Fig. 7 Temperature dependence of **a** electrical conductivity, **b** Seebeck coefficient and **c** Power factor for the 5% A-site deficiency La-SrTiO₃ ceramics sintered at different temperatures

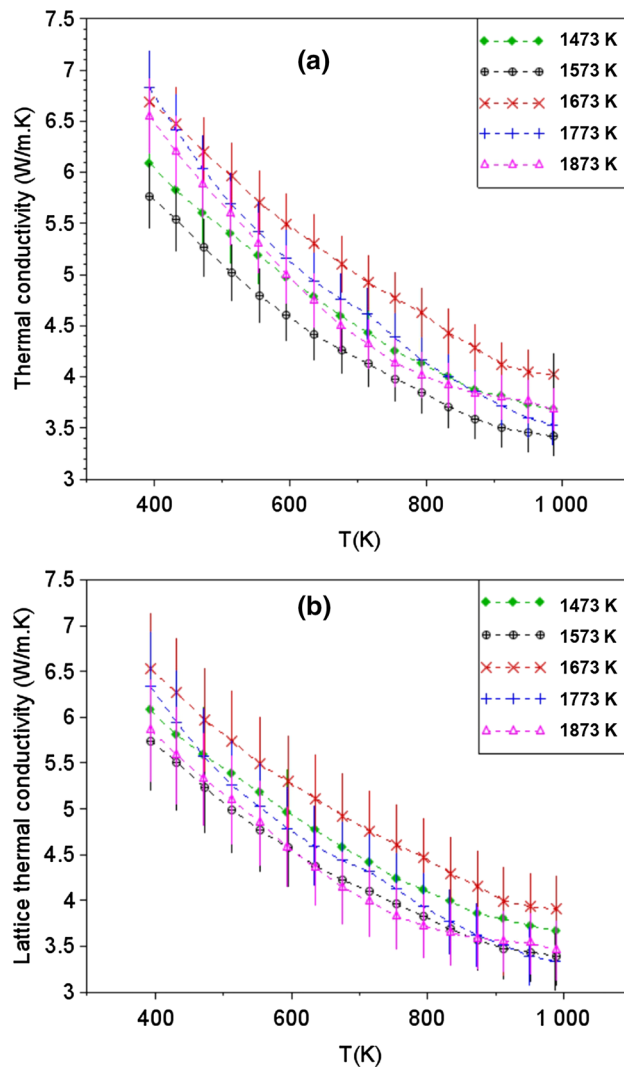


Fig. 8 Temperature dependence of the thermal conductivity **(a)** and lattice thermal conductivity **(b)** for the 5% A-site deficiency La-SrTiO₃ ceramics sintered at different temperatures

tionally sintered samples [35, 53] but similar to those reported by Singh et al. [20] for samples with micrometer grains sintered by SPS. These results are consistent with Loland et al. [46], who didn't observe significant effect of the rutile phase on thermal conductivity.

The calculated ZT values of the as-sintered ceramics are shown in Fig. 9. One can see a significant improvement on ZT values with respect to sintering temperature. The figure of merit was increased by approximately tenfold than the one sintered at 1473 K. Owing to the increase in the power factor, the ZT value was enhanced.

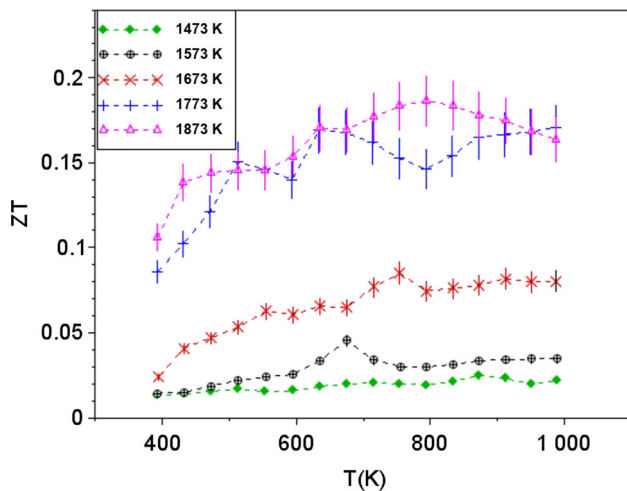


Fig. 9 Temperature dependence of ZT value for the 5% A-site deficiency La-SrTiO₃ ceramics sintered at different temperatures

Furthermore, the highest ZT ranging from 0.1 to 0.2 was achieved at low temperature (at 400 K), for (Sr_{0.95}La_{0.05})_{0.95}□_{0.05}TiO₃ compound sintered at 1873 K and remains almost constant in the whole measuring temperature range. Considering the A-site deficiency, and comparing with previous studies, one can see that the obtained results reveal a good agreement. For example, in the work reported by Lu et al. [35] and Azough et al. [55], the highest ZT value (0.2) at 800 K have been achieved for Sr_{0.84}La_{0.1}TiO_{3-δ}. Similarly, for Singh et al. [20], the highest ZT value (0.2) at 800 K was recorded for (Sr_{0.88}La_{0.12})_{0.95}TiO₃. This study clearly shows that the higher the sintering temperature, the higher the thermoelectric properties. Moreover, it has been shown that using a one step 10 min short SPS treatment leads to similar properties as a several-hours sintering step and a several-hours reducing atmosphere annealing step.

4 Conclusion

(Sr_{0.95}La_{0.05})_{0.95}□_{0.05}TiO₃ ceramics were prepared by solid state reaction and sintered by spark plasma sintering at different temperature ranging from 1473 to 1873 K for 10 min. The thermoelectric properties show that sintering at temperatures higher than 1773 K allows reaching high thermoelectric properties similar to the ones obtained after annealing at high temperatures in H₂/N₂ for several hours. Therefore, the 10 min short SPS process at high temperatures described in this paper is an easy, cheap, fast, and one step route to dense and efficient SrTiO₃-based thermoelectric ceramics. The microstructure observations by SEM show that titanium oxide phases are present as well as some lanthanum compound aggregates. Therefore, the 5% La substitution that usually exhibits the best thermoelectric properties for SrTiO₃ is probably not the most

appropriate concentration for A-vacancy-Sr-titanates sintered by this process and further studies to find the optimum thermoelectric properties have to be undertaken.

Acknowledgements The authors are grateful to Tatiana Chartier for technical support.

References

1. I. Terasaki, Y. Sasago, K. Uchinokura, Large thermoelectric power in NaCo₂O₄ single crystals. *Phys. Rev. B* **56**, R12685–R12687 (1997)
2. J.W. Fergus, Oxide materials for high temperature thermoelectric energy conversion. *J. Eur. Ceram. Soc.* **32**, 525–540 (2012)
3. M.W. Gaultois, T.D. Sparks, C.K.H. Borg, R. Seshadri, W.D. Bonificio, Data-driven review of thermoelectric materials: performance and resource considerations. *Chem. Mater.* **25**, 2911–2920 (2013)
4. M. Shikano, R. Funahashi, Electrical and thermal properties of single-crystalline (Ca₂CoO₃)_{0.7}CoO₂ with a Ca₃Co₄O₉ structure. *Appl. Phys. Lett.* **82**, 1851–1853 (2003)
5. A.C. Masset, C. Michel, A. Maignan, M. Hervieu, O. Toulemonde, F. Studer, B. Raveau, J. Hejtmanek, Misfit-layered cobaltite with an anisotropic giant magnetoresistance: Ca₃Co₄O₉. *Phys. Rev. B* **62**, 166–175 (2000)
6. F. Delorme, C. Chen, B. Pignon, F. Schoenstein, L. Perriere, F. Giovannelli, Promising high temperature thermoelectric properties of dense Ba₂Co₉O₁₄ ceramics. *J. Eur. Ceram. Soc.* **37**, 2615–2620 (2017)
7. G. Constantinescu, S. Rasekh, M.A. Torres, M.A. Madre, J.C. Diez, A. Sotelo, Enhancement of the high-temperature thermoelectric performance of Bi₂Ba₂Co₂O_x ceramics. *Scr. Mater.* **68**, 75–78 (2013)
8. A.I. Klyndyuk, N.S. Krasutskaya, E.A. Chizhova, Synthesis and thermoelectric properties of ceramics based on Bi₂Ca₂Co_{1.7}O_y oxide. *Phys. Chem. Glas.* **44**, 100–107 (2018)
9. J. Androulakis, P. Migiakis, J. Giapintzakis, La_{0.95}Sr_{0.05}CoO₃: an efficient room-temperature thermoelectric oxide. *Appl. Phys. Lett.* **84**, 1099–1101 (2004)
10. H. Kozuka, K. Yamagiwa, K. Ohbayashia, K. Koumoto, Origin of high electrical conductivity in alkaline-earth doped LaCoO₃. *J. Mater. Chem.* **22**, 11003–11005 (2012)
11. C. Chen, F. Giovannelli, T. Chartier, F. Delorme, Synthesis and thermoelectric properties of doubly substituted La_{0.95}Sr_{0.05}Co_{1-x}Cr_xO₃ (0 ≤ x ≤ 0.5). *Mater. Res. Bull.* **102**, 257–261 (2018)
12. M.A. Bousnina, R. Dujardin, L. Perriere, F. Giovannelli, G. Guegan, F. Delorme, Synthesis, sintering, and thermoelectric properties of the solid solution La_{1-x}Sr_xCoO_{3±δ} (0 ≤ x ≤ 1). *J. Adv. Ceram.* **7**, 160–168 (2018)
13. C. Chen, F. Delorme, F. Schoenstein, M. Zaghioui, D. Flahaut, J. Allouche, F. Giovannelli, Synthesis, sintering

- and thermoelectric properties of $\text{Co}_{1-x}\text{M}_x\text{O}$ ($\text{M} = \text{Na}$, $0 \leq x \leq 0.07$; $\text{M} = \text{Ag}$, $0 \leq x \leq 0.05$). *J. Eur. Ceram. Soc.* **39**, 346–351 (2019)
14. M. Ohtaki, T. Tsubota, K. Eguchi, H. Arai, High-temperature thermoelectric properties of $(\text{Zn}_{1-x}\text{Al}_x)\text{O}$. *J. Appl. Phys.* **79**, 1816–1818 (1996)
 15. D. Flahaut, T. Mihara, R. Funahashi, N. Nabeshima, K. Lee, H. Ohta, K. Kumihito, Thermoelectrical properties of A-site substituted $\text{Ca}_{1-x}\text{Re}_x\text{MnO}_3$ system. *J. Appl. Phys.* **100**, 4 (2006)
 16. T. Okuda, K. Nakanishi, S. Miyasaka, Y. Tokura, Large thermoelectric response of metallic perovskites: $\text{Sr}_{1-x}\text{La}_x\text{TiO}_3$ ($0 < x < 0.1$). *Phys. Rev. B* **63**, 113104 (2001)
 17. H. Muta, K. Kurosaki, S. Yamanaka, Thermoelectric properties of rare earth doped SrTiO_3 . *J. Alloys Compd.* **350**, 292295 (2003)
 18. J. Wang, B.Y. Zhang, H.J. Kang, Y. Li, X. Yaer, J.F. Li, Q. Tan, S. Zhang, G.H. Fan, C.Y. Liu, L. Miao, D. Nan, T.M. Wang, L.D. Zhao, Record high thermoelectric performance in bulk SrTiO_3 via nano-scale modulation doping. *Nano Energy* **35**, 387–395 (2017)
 19. D. Srivastava, C. Norman, F. Azough, M.C. Schäfer, E. Guilmeau, D. Kepaptsoglou, Q.M. Ramasse, G. Nicotra, R. Freer, Tuning the thermoelectric properties of A-site deficient SrTiO_3 ceramics by vacancies and carrier concentration. *Phys. Chem. Chem. Phys.* **18**, 26475–26486 (2016)
 20. S.P. Singh, N. Kanas, T.D. Desissa, M. Johnsson, M.-A. Einarsrud, T. Norby, K. Wiik, Thermoelectric properties of A-site deficient La-doped SrTiO_3 at 100–900 °C under reducing conditions. *J. Eur. Ceram.* **40**, 401–407 (2020)
 21. S. Ohta, T. Nomura, High-temperature carrier transport and thermoelectric properties of heavily La- or Nb-doped SrTiO_3 single crystals. *J. Appl. Phys.* **97**, 034106 (2005)
 22. C. Chen, T. Zhang, R. Donelson, T. Teck Tan, S. Lia, Effects of yttrium substitution and oxygen deficiency on the crystal phase, microstructure, and thermoelectric properties of $\text{Sr}_{1-1.5x}\text{Y}_x\text{TiO}_{3-\delta}$ ($0 \leq x \leq 0.15$). *J. Alloys Compd.* **629**, 49–54 (2015)
 23. L. Zhang, T. Tosho, N. Okinaka, T. Akiyama, Thermoelectric properties of combustion synthesized and spark plasma sintered $\text{Sr}_{1-x}\text{R}_x\text{TiO}_3$ ($\text{R} = \text{Y}$, La , Sm , Gd , Dy , $0 < x \leq 0.1$). *Mater. Trans.* **48**, 2088–2093 (2007)
 24. A.M. Dehkordi, S. Bhattacharya, J. He, H.N. Alsharief, T.M. Tritt, Significant enhancement in thermoelectric properties of polycrystalline Pr-doped $\text{SrTiO}_{3-\delta}$ ceramics originating from nonuniform distribution of Pr dopants. *Appl. Phys. Lett.* **104**, 193902 (2014)
 25. C. Chen, M. Bousnina, F. Giovannelli, F. Delorme, Influence of Bi on the thermoelectric properties of $\text{SrTiO}_{3-\delta}$. *J. Materiomics* **5**, 88–93 (2019)
 26. A.A. Yaremchenko, S. Populoh, S.G. Patrício, J. Macías, P. Thiel, D.P. Fagg, A. Weidenkaff, J.R. Frade, A.V. Kovalevsky, Boosting thermoelectric performance by controlled defect chemistry engineering in Ta-substituted strontium titanate. *Chem. Mater.* **27**, 4995–5006 (2015)
 27. N. Wang, H. He, X. Li, L. Han, C. Zhang, Enhanced thermoelectric properties of Nb-doped SrTiO_3 polycrystalline ceramic by titanate nanotube addition. *J. Alloys Compd.* **506**, 293–296 (2010)
 28. M.S. Toprak, C. Stiewe, D. Platzek, S. Williams, L. Bertini, E. Muller, C. Gatti, Y. Zhang, M. Rowe, M. Muhammed, The impact of nanostructuring on the thermal conductivity of thermoelectric CoSb_3 . *Adv. Funct. Mater.* **14**, 1189–1196 (2004)
 29. S. Perumal, S. Roychowdhury, K. Biswas, Reduction of thermal conductivity through nanostructuring enhances the thermoelectric figure of merit in $\text{Ge}_{1-x}\text{Bi}_x\text{Te}$. *R. Soc. Chem.* **3**, 125–132 (2016)
 30. N. Wang, H. Chen, H. He, W. Norimatsu, M. Kusunoki, K. Koumoto, Enhanced thermoelectric performance of Nb-doped SrTiO_3 by nano-inclusion with low thermal conductivity. *Sci. Rep.* **3**, 1–5 (2013)
 31. K. Park, J.S. Son, S.I. Woo, K. Shin, M.W. Oh, S.D. Park, T. Hyeon, Colloidal synthesis and thermoelectric properties of La-doped SrTiO_3 nanoparticles. *J. Mater. Chem.* **2**, 4217–4224 (2014)
 32. H. Ohta, S. Kim, Y. Mune, T. Mizoguchi, K. Nomura, S. Ohta, T. Nomura, Y. Nakanishi, Y. Ikuhara, M. Hirano, Giant thermoelectric Seebeck coefficient of a two-dimensional electron gas in SrTiO_3 . *Nat. Mater.* **6**, 129–134 (2007)
 33. F. Giovannelli, C. Chen, P. Díaz-Chao, E. Guilmeau, F. Delorme, Thermal conductivity and stability of Al-doped ZnO nanostructured ceramics. *J. Eur. Ceram.* **38**, 5015–5020 (2018)
 34. A.V. Kovalevsky, A.A. Yaremchenko, S. Populoh, A. Weidenkaff, J.R. Frade, Effect of A-site cation deficiency on the thermoelectric performance of donor-substituted strontium titanate. *J. Phys. Chem. C* **118**, 4596–4606 (2014)
 35. Z. Lu, H. Zhang, W. Lei, D.C. Sinclair, I.M. Reaney, High-figure-of-merit thermoelectric La-doped A-site-deficient SrTiO_3 ceramics. *Chem. Mater.* **28**, 925–935 (2016)
 36. J. Han, Q. Sun, Y. Son, Enhanced thermoelectric properties of La and Dy co-doped, Sr-deficient SrTiO_3 ceramics. *J. Alloys Compd.* **705**, 22–27 (2017)
 37. O. Okhay, S. Zlotnik, W. Xie, K. Orlinski, M.J. Hortiguera Gallo, G. Otero-Irurueta, A.J.S. Fernandes, D.A. Pawlak, A. Weidenkaff, A. Tkach, Thermoelectric performance of Nb-doped SrTiO_3 enhanced by reduced graphene and Sr deficiency cooperation. *Carbon* **143**, 215–222 (2019)
 38. A.V. Kovalevsky, M.H. Aguirre, S. Populoh, S.G. Patrício, N.M. Ferreira, S.M. Mikhalev, D.P. Fagg, A. Weidenkaff, J.R. Frade, Designing strontium titanate-based thermoelectrics: insight into defect chemistry mechanisms. *J. Mater. Chem. A* **5**, 3909–3922 (2017)
 39. Z.A. Munir, U. Anselmi-Tamburini, M. Ohyanagi, The effect of electric field and pressure on the synthesis and consolidation of materials: a review of the spark plasma sintering method. *J. Mater. Sci.* **41**, 763–777 (2006)
 40. A. Kikuchi, N. Okinaka, T. Akiyama, A large thermoelectric figure of merit of La-doped SrTiO_3 prepared by combustion synthesis with post-spark plasma sintering. *Scr. Mater.* **63**, 407–410 (2010)
 41. A. Kikuchi, L. Zhang, N. Okinaka, T. Tosho, T. Akiyama, Optimization of sintering temperature for maximizing dimensionless figure of merit of La-doped strontium titanate thermoelectric material in the com-

- bination of combustion synthesis with post spark plasma sintering. *Mater. Trans.* **51**, 1919–1922 (2010)
42. P. Roy, V. Pal, T. Maiti, Effect of Spark Plasma Sintering (SPS) on the thermoelectric properties of SrTiO₃: 15 at % Nb. *Ceram. Int.* **43**, 12809–12813 (2017)
 43. M. Acharya, S.S. Jana, M. Ranjan, T. Maiti, High performance ($ZT_{\text{r}} > 1$) n-type oxide thermoelectric composites from earth abundant materials. *Nano Energy* **84**, 2211–2855 (2021)
 44. E. Alleno, D. Bérardan, C. Byl, C. Candolfi, R. Daou, R. Decourt, E. Guilmeau, S. Hébert, J. Hejtmanek, B. Lenoir, P. Masschelein, V. Ogorodnichuk, M. Pollet, S. Populoh, D. Ravot, O. Rouleau, M. Soulier, Invited article: A round robin test of the uncertainty on the measurement of the thermoelectric dimensionless figure of merit of Co_{0.97}Ni_{0.03}Sb₃. *Rev. Sci. Instrum.* **86**, 011301 (2015)
 45. J. Liu, H.C. Wang, W.B. Su, C.L. Wang, J.L. Zhang, L.M. Mei, Synthesis and thermoelectric properties of Sr_{0.95}La_{0.05}TiO_{3- δ} -TiO₂ solid solutions. *Solid State Sci.* **12**, 134–137 (2010)
 46. T.E. Loland, J. Sele, M. Einarsrud, P.E. Vullum, M. Johnsson, K. Wiik, Thermal conductivity of A-site cation-deficient La-substituted SrTiO₃ produced by spark plasma sintering. *Energy Harvest. Syst.* **2**, 63–71 (2015)
 47. A.M. Dehkordi, S. Bhattacharya, T. Darroudi, J.W. Graff, U. Schwingenschlögl, H.N. Alshareef, T.M. Tritt, Large thermoelectric power factor in Pr-doped SrTiO_{3- δ} ceramics via grain-boundary-induced mobility enhancement. *Chem. Mater.* **26**, 2478–2485 (2014)
 48. S. Yamanaka, K. Kurosaki, T. Maekawa, T. Matsuda, S. Kobayashi, M. Uno, Thermochemical and thermophysical properties of alkaline-earth perovskites. *J. Nucl. Mater.* **344**, 61–66 (2005)
 49. A. Rocca, A. Licciulli, M. Politi, D. Diso, Rare Earth-doped SrTiO₃ perovskite formation from Xerogels. *ISRN Ceram.* **2012**, 926537 (2012)
 50. G.J. Synder, E.S. Toberer, Complex thermoelectric materials. *Nat. Mater.* **7**, 105–114 (2008)
 51. J. Cao, D. Ekren, Y. Peng, F. Azough, I.A. Kinloch, R. Freer, Modulation of charge transport at grain boundaries in SrTiO₃: toward a high thermoelectric power factor at room temperature. *ACS Appl. Mater. Interfaces* **13**, 11879–11890 (2021)
 52. C. Wu, J. Li, Y. Fan, J. Xing, H. Gu, Z. Zhou, X. Lu, Q. Zhang, L. Wang, W. Jiang, The effect of reduced graphene oxide on microstructure and thermoelectric properties of Nb-doped A-site-deficient SrTiO₃ ceramics. *J. Alloys Compd.* **786**, 884–893 (2019)
 53. S.R. Popuri, A.J.M. Scott, R.A. Downie, M.A. Hall, E. Suard, R. Decourt, M. Pollet, J.-W.G. Bos, Glass-like thermal conductivity in SrTiO₃ thermoelectrics induced by A-site vacancies. *RSC Adv.* **4**, 33720–33723 (2014)
 54. P.C. Sharma, K.S. Dubey, G.S. Verma, Three-phonon scattering and Guthrie's limits for its temperature dependence. *Phys. Rev. B.* **4**, 1306–1313 (1971)
 55. F. Azough, S.S. Jackson, D. Ekren, R. Freer, M. Molinari, S.R. Yeandel, P.M. Panchmatia, S.C. Parker, D.H. Maldonado, D.M. Kepaptsoglou, Q.M. Ramasse, Concurrent La and A-site vacancy doping modulates the thermoelectric response of SrTiO₃: experimental and computational evidence. *ACS Appl. Mater. Interfaces* **9**, 41988–42000 (2017)